OPTIMIZING HYDRAULIC RESERVOIRS USING EULER-EULER-LAGRANGE MULTIPHASE CFD SIMULATION

Lukas Muttenthaler*, Bernhard Manhartsgruber

Institute of Machine Design and Hydraulic Drives, Johannes Kepler University, Altenbergerstrasse 69, 4040 Linz
* Corresponding author: Tel.: +43 732 2468 6526; E-mail address: lukas.muttenthaler@gmail.com

ABSTRACT

Well working hydraulic systems need clean hydraulic oil. Therefore, the system must ensure the separation of molecular, gaseous, liquid and solid contaminations. The key element of the separation of contaminants is the hydraulic reservoir.
Solid particles are a major source of maintenance costs and machine downtime. Thus, an Euler-Euler-Lagrange multiphase CFD model to predict the transport of solid particles in hydraulic reservoirs was developed. The CFD model identifies and predicts the particle accumulation areas and is used to train port-to-port transfer functions, which can be used in system models to simulate the long-term contamination levels of hydraulic systems. The experimental detection of dynamic particle contamination levels and particle accumulation areas validate and confirm the CFD and the system model.

Both models in combination allow for parameter and design studies to improve the fluid management of hydraulic reservoirs.

Keywords: Hydraulic Reservoir, Particle Contamination, Multiphase CFD Simulation, Optimization

1. INTRODUCTION

Due to the huge impact of hydraulic reservoirs on the fluid properties, the reservoirs must meet certain requirements in modern hydraulic systems. These fluid properties influence the system stiffness, repeatability, components lubrication, wear, noise, machine downtime and fluid degradation.

The hydraulic reservoir is responsible for the separation of solid, liquid, gaseous and molecular contaminations and temperature management directly or indirectly.

The design of the hydraulic reservoir including its inlets and outlets defines the fluid flow. The contaminated and heated hydraulic oil from the system must be cooled and the contaminations must be separated and filtered.

The portion of damages caused by solid contamination is up to 85 % [1]. To halve the number of solid particles in a hydraulic system increases the lifetime of the components by a factor of $1.1 - 1.5$ [2].

Modern approaches use sensor technology and condition monitoring algorithms to observe fluid properties to improve the machine lifetime and reduce machine downtimes and maintenance costs. [3, 4]

Experimental investigations showed the effect of different oil and air flow rates and different reservoir designs on air separation efficiency. [5]

These experiments were the starting point for the development of Euler-Lagrangian CFD codes to simulate and therefore to predict the behavior of air bubbles in hydraulic reservoirs [6, 7]. To avoid expensive and protracted CFD simulations the CFD codes were used to develop a metamodel. [8]

Multiphase CFD simulation enabled the combined investigation of air bubbles and solid particles in hydraulic reservoirs. The influence of the design of the hydraulic reservoir on air and particle separation was demonstrated and different active and passive techniques to improve the separation processes were tested. [9, 10]

Modelling and experimental quantification of particle sources and sinks, e.g. displacement units, cylinder seals, breather filters and oil filters allow for system theory-oriented considerations. [11, 12]

The particle contamination in hydraulic systems can be simulated using lumped-parameter models. In case of simple circuits analytical solutions can be found. More complex systems can be solved by numerical methods. [13, 14]

A systematization and an extensive lumped-parameter modelling of various components of hydraulic systems was done by von Dombrowski [15].

This study determines the particle accumulation areas including the quantification of the probabilities and the inlet-to-outlet transfer functions of particles. The Euler-Euler-Lagrange CFD model, which was developed and tested in [16], shows the particle accumulation areas and is the basis of the fitted system models. Both are compared with experimental results.

The particle accumulation areas and the transfer functions are determined for different particle diameters, reservoir designs and oil flow rates. The lumped-parameter model of the particles in the reservoir is discussed.

2. PROBLEM FORMULATION

The fundamental consideration of the multiphase CFD model is to describe the oil and air phase in the Eulerian and the solid particles in the Lagrangian way.

The Reynolds-averaged Navier-Stokes equations provide the stationary solution of the fluid phases, which are used as flow field to simulate the particle trajectories.

The Lagrangian particle tracking determines the trajectories of each particle and enables a specific view to the transport phenomena.

2.1. Fluid Phase

The volume of fluid method models the oil and air phases including the oil-air-interface. This method solves a single set of momentum equations and a transport equation for each phase. The material properties are represented by the volume fraction weighted average of the property of each phase.

The modelling of the turbulence is done by Menter's Shear Stress Transport model, which ensures good quality of flow results in the whole computational domain using the k-ω approach in wall regions and the k-ε model in free flow regions. Details of the used CFD model are given in [16].

2.2. Particle Phase

Local Particle Sedimentation Probability

Particle sets, or also called dusts, have different numbers of particles in each size class m, which are described by particle size density function $q_n(d_m)$.

Particle size density functions can express the ratio of quantity $q_0(d_m)$, diameter $q_1(d_m)$, cross section/surface $q_2(d_m)$ and volume/mass $q_3(d_m)$ in each size class.

Assuming spherical particles, these particle size density functions can be converted to each other using an integer power law:

$$q_n(d_m) = \frac{d_m^{n-r}\, q_r(d_m)}{\sum_s d_s^{n-r}\, q_r(d_s)\, \Delta d_s} \quad (1)$$

The width of the fraction s is given by Δd_s and n and r characterizes the power law exponents.

Each size class in the CFD simulation is represented by the same number of particles. The local sedimentation probability $f_{n,frac}(x_i, x_j, d_s)$, which is the result of the CFD simulation, can be transformed to get the particle sedimentation probability of a dust $f_{n,t}(x_i, x_j)$ with specific size distribution:

$$f_{n,t}(x_i, x_j) = \sum_s f_{n,frac}(x_i, x_j, d_s)\, q_n(d_s) \quad (2)$$

Dynamic Particle System Model

Lumped-parameter models can describe the transient behaviour of particle sets in a hydraulic system.

To characterize the dynamics of particle sets in a hydraulic reservoir the diameter-dependent mass balance of the change of not-sedimented particles for the reservoir $\dot{m}_{R,d}$ can be written as:

$$\dot{m}_{R,d}(t) = \dot{m}_{In,d}(t) - \dot{m}_{Out,d}(t) - \dot{m}_{S,d}(t) \quad (3)$$

The index d specifies, that the physical quantity is diameter dependent.

The mass flow rate at inlet $\dot{m}_{In,d}(t)$ and outlet $\dot{m}_{Out,d}(t)$ can be expressed by:

$$\dot{m}_{In,d}(t) = c_{In,d}(t)\, Q_{In}(t) \quad (4)$$

$$\dot{m}_{Out,d}(t) = c_{R,d}\,(t)\, Q_{Out}(t) = c_{Out,d}\,(t)\, Q_{Out}(t) \quad (5)$$

The particle mass $\dot{m}_{In,d}$, which enters the reservoir is a function of the particle mass

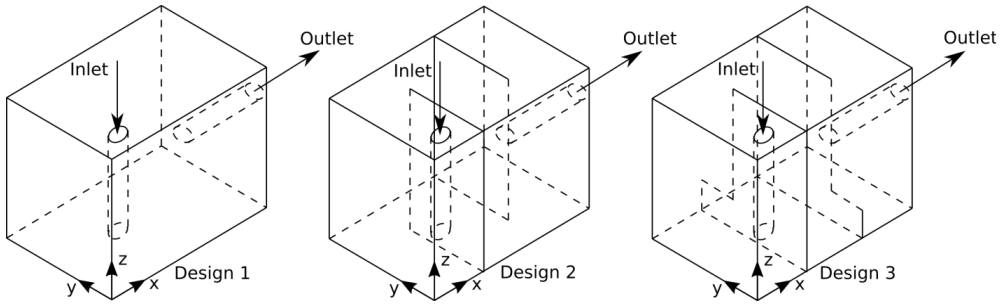

Figure 1: Design of hydraulic reservoirs

$\dot{m}_{Out,d}$, which leaves the reservoir and an additional term $\dot{m}_{Sys,d}$, which represents the net balance of particle sinks and sources in the hydraulic system (except the reservoir):

$$\dot{m}_{In,d}(t) = \dot{m}_{Out,d}(t) + \dot{m}_{Sys,d}(t) \quad (6)$$

Let the inlet and outlet fluid flow be equal and constant. Therefore, filling height h_R and filling volume V_R are constant.

The net mass source referenced to the fluid flow of the system:

$$\dot{m}_{Sys,d}(t) = \mathrm{c_{Sys,d}}(t)\, Q_{Sys} \quad (7)$$

Assume particles entering the reservoir are mixed perfectly along the vertical axis, the sedimentation rate $\dot{m}_S$ is:

$$\dot{m}_{S,d}(t) = \frac{m_{R,d}(t)}{t_{max,d}} = m_{R,d}(t)\ \frac{v_{S,d}}{h_R} \quad (8)$$

The mass sedimentation rate is proportional to the terminal velocity of a falling spherical particle $v_{S,d}$ in a Stokes regime [17]:

$$v_{S,d} = \frac{(\rho_P - \rho)\, g\, d_P^2}{18\, \eta} \quad (9)$$

Inserting Equation 4, 5 and 8 in Equation 3 results in:

$$\dot{m}_{R,d}(t) = \dot{m}_{Sys,d}(t) - m_{R,d}(t)\ \frac{v_{S,d}}{h_R} \quad (10)$$

Expressing Equation 10 in particle state per unit volume and insertion of Equation 7 lead to:

$$\dot{c}_{R,d}(t)\ \mathrm{V_R} = \mathrm{c_{Sys,d}}(t)\, Q_{Sys} - c_{R,d}(t)\ \mathrm{V_R}\ \frac{v_{S,d}}{h_R} \quad (11)$$

Equation 11 is a first order linear differential equation with constant coefficients. Thus, the transfer function with $c_{Sys,d}$ as input and $c_{R,d} = c_{Out,d}$ as output is defined:

$$G_d(s) = \frac{\mathrm{C}_{R,d}(s)}{C_{Sys,d}(s)} = \frac{K_d}{1 + T_{t,d}\ s} \quad (12)$$

The implicit assumption, that particles entering the hydraulic reservoir are mixed immediately in horizontal direction is expressed by Equation 12. Therefore, particles entering the hydraulic reservoir would result in particle fractions, which leave the reservoir without time delay.

Thus, the dead time $T_{d,d}$ is introduced and can be represented by an delay, which means to replace $\dot{c}_{Sys,d}(t)$ by $\dot{c}_{Sys,d}(t - T_{d,d})$:

$$G(s) = \frac{\mathrm{C}_{R,d}(s)}{C_{Sys,d}(s)} = \frac{K_d}{1 + T_{t,d}\ s}\ e^{-T_{d,d}\, t} \quad (13)$$

The introduction of a dead time $T_{d,d}$ is well defined. Because in case of an unknown flow an a priori estimation of the dead time can be done by using the minimum geometric possible way length l_{min} and a representative mean flow velocity $v_{flow,rep}$ in the hydraulic reservoir:

$$T_{d,d} \approx \frac{l_{min}}{v_{flow,rep}} \quad (14)$$

3. SIMULATION AND EXPERIMENTAL SETUP

Figure 1 deals with the designs of the hydraulic reservoirs. The first design does not use baffles, whereas the second one uses two baffles to direct the flow and third one uses baffles with thresholds on the ground.

The hydraulic reservoir with the coordinate axes, the section planes, and the applied sensors, pumps and other hardware are shown in **Figure 2**.

The volume flow, the pressure, the temperature and the particle contamination levels of different particle size classes are measured. The main flow can be varied by a variable-speed motor.

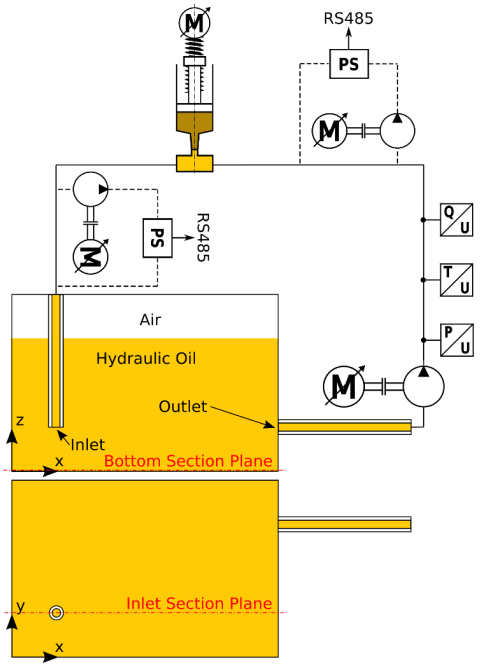

Figure 2: Front and top view of setup

The dimensions of the hydraulic reservoir are listed in **Table 1.** The outer dimensions of the reservoirs are the same for all three considered designs.

Table 1: Geometry of Hydraulic Reservoir

Parameter naming	Value
Basic dimensions $l_x \times l_y \times l_z$	$0.3 \times 0.2 \times 0.2$ m
Inlet/outlet pipe diameter d_{Pipe}	14 mm
Inlet/Outlet pipe length l_I, l_O	150 mm, 140 mm
Inlet pipe axis center x_I, y_I	50 mm, 50 mm
Outlet pipe axis center y_O, z_O	150 mm, 50 mm
Baffle positions x_{B1}, x_{B2}	100 mm, 200 mm
Baffle opening width y_B	35 mm
Baffle threshold height z_B	35 mm

3.1. Simulation Setup

All multiphase CFD simulations are done by ANSYS Fluent 18.2.

The simulation of the fluid flow is done with constant boundary conditions and the simulation aborts after converging to the steady solution.

Then the particle trajectories are calculated, whereby two different sets of particles are considered. One set has their start points on the ground. This set quantifies the particle accumulation areas. The other set starts at the inlet port and is used to determine the transfer function between the ports.

The procedure of the simulation of the fluid flows and the particle trajectories is shown in **Figure 3**.

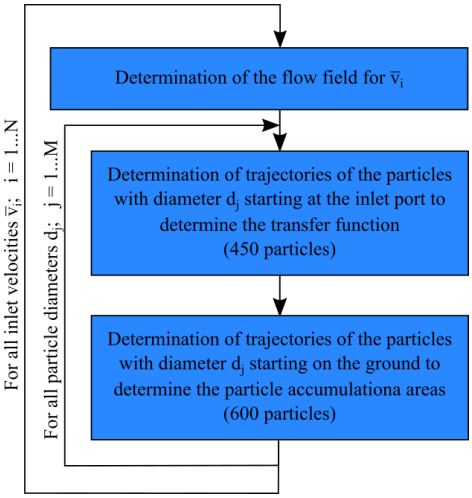

Figure 3: Simulation procedure

Only a short summary of the simulation setup is given in this paper. A detailed description of physical and numerical parameters including explanations of the simulation setup can be found in [16].

Fluid Phase

A parabolic velocity profile is defined as the boundary condition at inlet and outlet ports. The mean velocity is varied in the range of $\bar{v} = 0.05 - 4.0$ m/s.

The top plate was defined as constant pressure boundary condition. All velocity and pressure boundary conditions are set to 4% turbulence.

Due to high density ratio across the oil-air-interface the turbulence damping was enabled, to correct the expected high velocity gradients.

The low-Re correction, the curvature correction and the Kato-Launder limiter are enabled. The surface tension is also considered.

Particle Phase

The particle trajectories were determined in stationary flow fields. Particle sets with diameters in the range $d = 2 - 175$ µm are considered. 450 particles of each diameter starting at the inlet port

and 600 particles starting on the ground represents the particle contamination. Both sets are evenly distributed across the inlet port and on the ground, respectively.

The particles do not interact among each other and have no effect to the fluid flow because of the very low particle volume fraction. Typical particle contaminations in hydraulic systems are several orders of magnitude below 1.

Gravity, virtual mass force, pressure gradient force and a spherical drag law are considered. The collision of particles on the wall is modelled inelastic on the ground and elastic for all other walls.

The mesh consists of about 400 000 cells and is fully structured. To check the mesh convergence simulations with about 1 200 000 cells are done.

3.2. Experimental Setup

The experimental setup is shown in **Figure 4**. The hydraulic reservoir and the inlet and outlet pipes are made of PMMA. A magnetically-coupled centrifugal pump with variable frequency drive is responsible for the fluid flow.

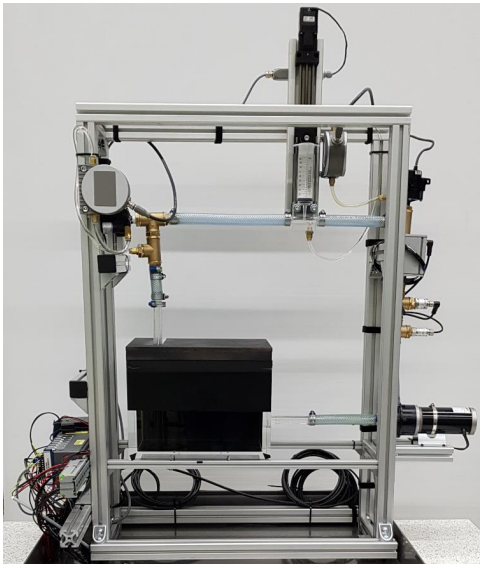

Figure 4: Experimental setup

Two further centrifugal pumps are responsible for the volume flow through particle sensors CS1210 from HYDAC. The sensors measure the cumulative particle quantity for particles with diameters $d_P > 4\ \mu m, 6\ \mu m, 14\ \mu m$ and $21\ \mu m$.

Particles are injected by an automatic dosing system, which consists of a stepper drive, a spindle and a syringe filled with a premixed oil-particle suspension. The particle and oil volumes in the syringe are known. Thus, the injected particle mass and concentration is known.

The hydraulic connections are done with flexible and transparent hoses.

Table 2 lists the material properties of the fluids and particles, which are used in simulations and experiments.

Table 2: Material properties

Parameter naming	Value
Temperature T	28 °C
Oil density ρ_{Oil}	$867\ kg/m^3$
Oil viscosity η_{Oil}	$46.3 * 10^{-3}$ Pa s
Air density ρ_{Air}	$1.149\ kg/m^3$
Air viscosity η_{Air}	$18.69 * 10^{-6}$ Pa s
Particle density ρ_P	$3950\ kg/m^3$

The aluminum oxide test dust particle size distribution is ‘fine’ according to ISO 12103-1:2016-04 A2. [18]

To determine the particle accumulation areas and the transfer functions, two sets of experiments were done.

In the first set of experiments the premixed oil-particle suspension is injected in the constant oil flow with the dosing system. During the experiments an online measurement of the particle quantities was done. The determined transfer functions are compared to the transfer functions determined by CFD simulations.

In the second set of experiments the particles were mixed with the oil in the test bench. A sedimentation time of 120 h enables the particles to sediment. During this period no flow is applied to the testbench.

After this sedimentation time a constant oil flow is applied for 10 min and then the particle accumulation areas are identified.

4. RESULTS AND DISCUSSION

4.1. Fluid Phase

Figure 5 shows that the left side of the hydraulic reservoir is dominated by the downwards jet caused by the inlet flow with a mean flow velocity of $\bar{v} = 1\ m/s$. The not confined vortex affects more than half of the hydraulic reservoir.

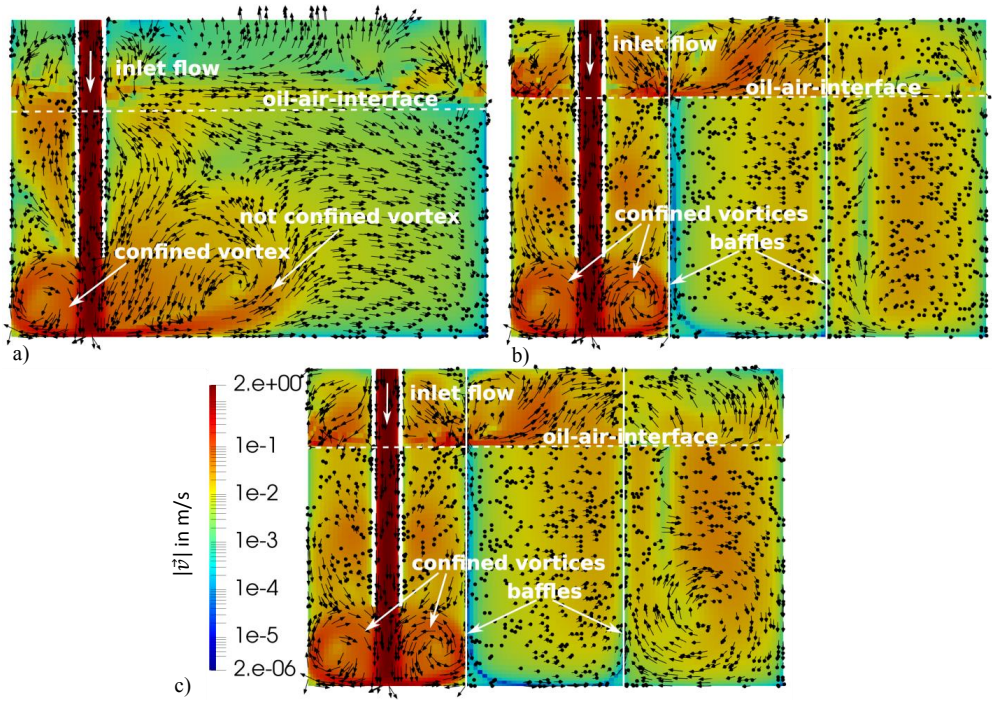

Figure 5: Velocity magnitude $|\vec{v}|$ in m/s on the inlet section plane; $\bar{v} = 1.0$ m/s (a) D1 (b) D2 (c) D3

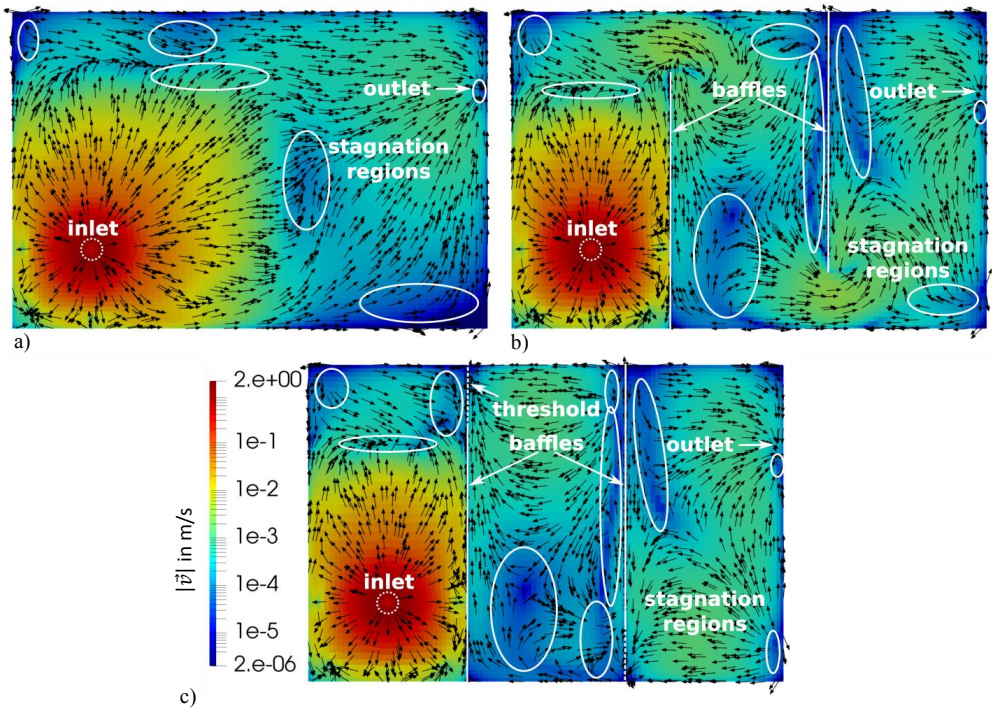

Figure 6: Velocity magnitude on the bottom section plane; $\bar{v} = 1.0$ m/s (a) D1 (b) D2 (c) D3

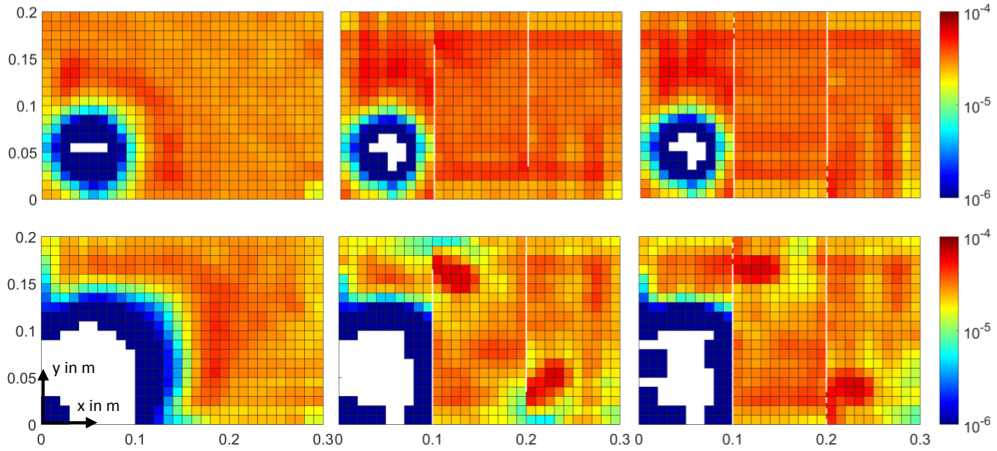

Figure 7: Local cross section-weighted particle sedimentation probability on the bottom; (top) $\bar{v} = 0.25$ m/s (bottom) $\bar{v} = 1.0$ m/s; (left) D1 (middle) D2 (right) D3

The cases with baffles show that the momentum of the inlet jet is contained in the first chamber and confined vortices occur. Sector 2 and 3 are not influenced by the inlet jet, which results in smoother flow.

The velocity magnitude of the air is quite high, due to high density ratio. Therefore, the production of turbulence kinetic energy is high, which leads to high velocity magnitudes.

The influence of the inlet jet to the flow on the ground is shown in **Figure 6** for the same inlet flow characterized by $\bar{v} = 1$ m/s. Without baffles the jet affects half of the ground area.

The jet can affect up to a 2/3 of the ground in case of high flow rates represented by $\bar{v} = 4$ m/s [16].

The baffles reduce the ground area affected by the jet to a quarter of the total area. The thresholds on the ground reduce the ground velocity and are an obstacle for particles creeping on the ground.

4.2. Particle Phase

Local Particle Sedimentation Probability

The ground of the hydraulic reservoirs in **Figure 7** is divided into 10 mm × 10 mm sections, which results in a 30 × 20 grid.
The sedimented particles in each section are counted in the post-processing, which leads to the $q_0(d_m)$-weighted particle sedimentation probability.

To transform the quantity- to the cross section-weighted particle sedimentation probability, shown in **Figure 7**, the transformation from the $q_0(d_m)$ to the $q_2(d_m)$-weighted particle size density function, according to Equation 1, was used. The transformation makes it possible to compare the results with optical experiments.
The upper row of **Figure 7** shows the simulated sedimentation probability in case of $\bar{v} = 0.25$ m/s, whereas the lower row shows the simulation results for $\bar{v} = 1$ m/s. The starting points of the particles are on the ground and are cartesian equally distributed.

All designs and flow velocities show an area beneath the inlet, where the particles are washed away. The size of this area depends on the flow velocity, the design of the reservoir and the particle size.

In cases with baffles the inlet jet is contained by the side walls and the first baffle and thus the area where particles are washed away is also contained.

Resuspended particles accumulate at spots with small velocities. Without baffles a ring around the inlet occurs where the resuspended particles beneath the inlet resediment.

In case of thresholds the velocity on the bottom can be reduced and so more particles resediment.

The comparison of **Figure 6** and **Figure 7** shows that the particle sedimentation regions correspond with the stagnation regions as

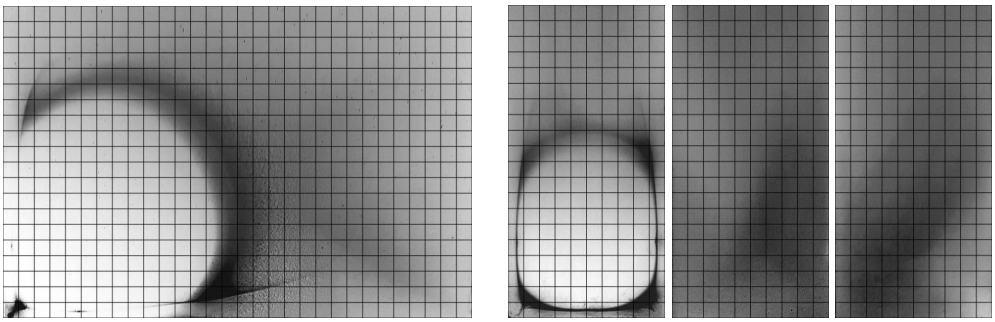

Figure 8: Experimentally determined local cross section-weighted particle sedimentation probability on the bottom; $\bar{v} = 1.0\ \mathrm{m/s}$ (left) D1 (right) D3

described in detail by Muttenthaler and Manhartsgruber [16].

Figure 8 shows postprocessed photos from sedimented particles. The colors of the photos were desaturated, and the contrast was increased.

The same $10\ \mathrm{mm} \times 10\ \mathrm{mm}$ grid for better orientation as in Figure 7 is superimposed.

Figure 8 is divided into two parts. The left side shows the experimentally determined particle sedimentation probability for Design 1. Whereby a circular ring around the inlet occurs. The ring has the same dimension and intensity as in **Figure 7**. The ends of the circular ring are kinked in simulation and experiment. The left bottom corner shows a robust stagnation point where particles are accumulated. The right side shows a homogenous distribution of particles.

The subfigures on the right side show the particle sedimentation probability of the three chambers of Design 3. The left subfigure shows the inlet region where separation lines occur. The effect is dominant in the picture, but the lines become weaker, if the flow is applied longer (like on the left side). Particles accumulate in the corners.

The upper region of the inlet chamber shows few particles and in the middle and right chamber the particle quantity is higher, like **Figure 7**.

Dynamic Particle System Model

Figure 9 shows the comparison of the normalized particle transfer between inlet and outlet determined by CFD simulation, system model and measurements. The particle transfer behaviour between inlet and outlet is determined by CFD simulation and the parameters of $G(s)$ are estimated by least squares fitting. The measurements are plotted to validate the CFD simulation and the estimated transfer functions.

The inlet step is normalized to 1 for each size class and the step starts at $t = 0\ \mathrm{s}$.

The accordance of the models and the measurements is good. The flow rate and the diameter of the particles influences the gains K_d . Increasing flow rates raise the particle output K_d. The faster particles move through the reservoir, the less particles sediment. An increasing particle diameter results in less transferred particles, because the sedimentation velocity increases with the particle size.

The comparison of Design 1 and 3 show that Design 3 has higher separation rates (lower K_d) over all flow rates and particle sizes.

The simulated and measured time constants $T_{t,d}$ are in good agreement. In case of small flow rates, the measured time constant is lower than the simulated one.

The dead times $T_{d,d}$ are higher in Design 3 than in Design 1. Because the minimum geometric length l_{min} of Design 3 is greater. The simulated dead times underestimates the dead time of the measurements in Design 3. A possible reason is a not stationary solution, where particle switch between faster and slower flow paths.

5. SUMMARY AND OUTLOOK

The developed multiphase CFD model can predict particle accumulation areas and port-to-port transfer functions. The trajectories for particles with initial positions on the ground and across the inlet port were calculated correctly for a wide range of particle sizes and oil flow rates.

The actual study compares fluid flow with particle trajectories and identifies the particle

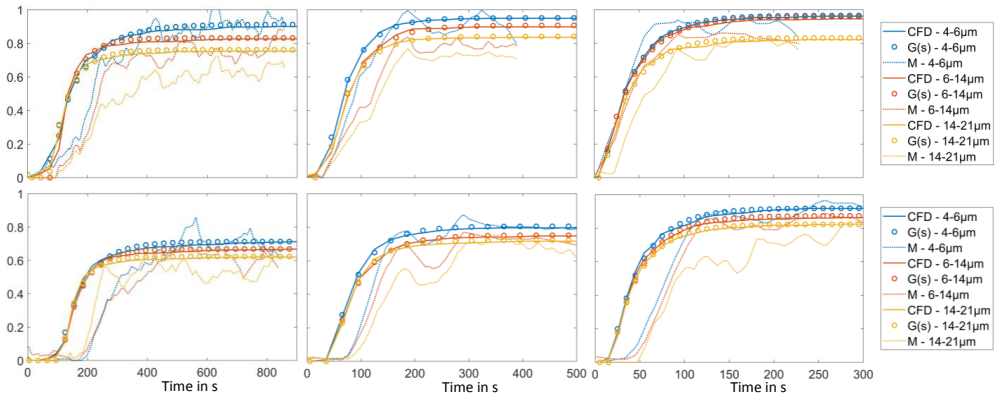

Figure 9: Dimensionless particle step response of hydraulic reservoir; (top) D1 (bottom) D3 (left) $\bar{v} = 0.25$ m/s (middle) $\bar{v} = 0.5$ m/s (right) $\bar{v} = 1.0$ m/s

accumulation areas and the parameters for the lumped-parameter model for different designs of hydraulic reservoirs.

The CFD simulation and the experimental results show a good qualitative accordance of particle accumulation areas and quantitative agreement of dynamic particle contamination levels.

In future, the measurement will be adapted to detect the particle contamination levels for more particle size classes.

The postprocessing of the detection of the accumulation areas will also be improved to make it easier to compare the measured and simulated accumulation areas.

Furthermore, a theory-oriented determination of the parameters of the lumped-parameter model will be done by analytical derivations and flow-based estimations.

Design changes like adding baffles, diffusors and other components to direct the flow can improve the separation behavior significantly.

Therefore, further analyses will apply the lumped-parameter and CFD models to more complex flow situations and geometries.

NOMENCLATURE

$c_{x,d}(t)$	Mass concentration of particles with diameter d at specified place x
d	Particle Diameter
d_{Pipe}	Inner diameter of inlet and outlet pipe
$f_{n,frac}(x_i, x_j, d_s)$	Local sedimentation probability of particle size class s at (x_i, x_j)
$f_{n,t}(x_i, x_j)$	Summed local weighted sedimentation probability of particle class s at (x_i, x_j)
$G_d(s)$	Diameter dependent particle transfer functions
g	Gravity
h_R	Oil filling height in the reservoir
K_d	Gain of PT1 system model
l_{min}	Minimum possible trajectory between inlet and outlet
l_I, l_O	Inlet/Outlet pipe lengths
$l_x \times l_y \times l_z$	Basic dimensions of hydraulic reservoir
$\dot{m}_{x,d}(t)$	Particle mass transport per time of diameter d at specified place x
Q_x	Fluid flow at specified point x
$q_n(d_m)$	Particle size density function of size class m
T	Temperature
$T_{d,d}$	Dead time of system model
$T_{t,d}$	Time constant of PT1 system model
t	Time
$t_{max,d}$	Maximum sedimentation time of particles with diameter d
V_R	Oil volume of the reservoir
$\bar{v}$	Mean flow velocity in the pipe
$\lvert\vec{v}\rvert$	Velocity magnitude of the fluid
$v_{S,d}$	Terminal sedimentation velocity of particles with diameter d
$v_{flow,rep}$	Representative fluid flow velocity
x_I, y_I, y_O, z_O	Inlet/Outlet pipe axis centres
x_i, x_j, x_k	Coordinate in x, y and z direction
η	Dynamic viscosity
ρ, ρ_P	Fluid/Particle density

REFERENCES

[1] Tič V, Lovrec D, Edler J (2012) Operation and accuracy of particle counters for online condition monitoring of hydraulic oils. Annals of Faculty Engineering Hunedoara – International Journal of Engineering, 12(3), 425-428

[2] C.C.Jensen A/S (2017). Clean Oil Guide. 9th edition. Svendborg, Denmark.

[3] Ng F, Harding JA, Glass J (2017) Improving hydraulic excavator performance through in line hydraulic oil contamination monitoring. Mechanical Systems and Signal Processing, 83, 176-193

[4] Dimmler G, Kilian FJ, Bader P, Muttenthaler L, Kapeller P (2018) So that the heart of the machine beats longer. Kunststoffe International, 10, 56-59

[5] Longhitano M, Protase A, Murrenhoff H (2016) Experimental Investigation of the Air Release in Hydraulic Reservoirs. In: Proceedings of the 10th International Fluid Power Conference. Dresden, Germany. March 8-10, 2016. 579-608

[6] Longhitano M, Murrenhoff H (2016) Prediction of Air Release in Hydraulic Reservoirs using Lagrangian Particle Tracking. In: Proceedings of the 9th International Conference on Multiphase Flow. Firenze, Italy. May 22-27, 2016.

[7] Mostafavi R, Tiffin D, Schmitz K (2018) Determination of the dynamic characteristic of a hydraulic reservoir for its air release efficiency using multiphase CFD model. In: Proceedings of the ASME/BATH 2018 Symposium on Fluid Power and Motion Control. Bath, UK. September 12–14, 2019. V001T01A008. ASME. doi.org/10.1115/FPMC2018-8813

[8] Mostafavi R, Schmitz K (2019) Development and Use of a Two-phase CFD Solver for Metamodeling of a Hydraulic Reservoir. Paper presented at the 10th International Conference on Multiphase Flow. Rio de Janeiro, Brazil. September 19–24, 2019. OC.080. ABCM

[9] Tič V, Lovrec D (2013) Air-release and solid particles sedimentation process within hydraulic reservoir. Tehnički vjesnik, 20(3), 407-412.

[10] Beckmann B, Laube M (2018) myCro – Downsizing of hydraulic power units by revolutionizing the design. In: Proceedings of the 11th International Fluid Power Conference. Aachen, Germany. March 19-21, 2018. 579-608

[11] Dahmann P (1992) Untersuchung der Feststoffpartikelkontamination in hydraulischen Systemen, RWTH Aachen University.

[12] Mager M (1999) Untersuchung der Feststoffpartikelkontamination in hydraulischen Systemen, RWTH Aachen University. Verlag Mainz, Aachen, Germany. ISBN 3-89653-266-9

[13] Foord BA (1978) Specifying fluid filtration through computer simulation. In: 34th Proceedings of the National Conference on Fluid Power. Philadelphia, PA, USA. November 7-9, 1978. 197-204

[14] Stecki JS, Chao L (1995) Modelling and Simulation of Contamination in Fluid Power Control Systems. In: Proceedings of the 4th Scandinavian International Conference on Fluid Power. Tampere, Finland. September 26-29, 1995. 356-368

[15] von Dombrowski R (2015) Modellierung der Partikelverteilung in hydraulischen Systemen, RWTH Aachen University. Shaker Verlag, Aachen, Germany. ISBN 978-8440-3744-9

[16] Muttenthaler L, Manhartsgruber B (2019) Prediction of particle resuspension and particle accumulation in hydraulic reservoirs using three-phase CFD simulations. In: Proceedings of the ASME/BATH 2019 Symposium on Fluid Power and Motion Control. Sarasota, Florida, USA. October 07–09, 2019. V001T01A008. ASME. doi.org/10.1115/FPMC2019-1617

[17] Lamb H (1879) Hydrodynamics. Cambridge University Press. Cambridge, UK.

[18] KSL Staubtechnik GmbH (2017) Sicherheitsdatenblatt Prüfstäube mit Korund. 1270-0 Edition. Lauingen, Germany.